SANDIA REPORT

SAND2008-1333
Unlimited Release
Printed February 2008

Final LDRD Report: Infrared Detection and Power Generation Using Self-Assembled Quantum Dots

Jeffrey G. Cederberg, Eric A. Shaner, and A. Robert Ellis

Prepared by
Sandia National Laboratories
Albuquerque, New Mexico 87185 and Livermore, California 94550

Sandia National Laboratories

Issued by Sandia National Laboratories, operated for the United States Department of Energy by Sandia Corporation.

Available to DOE and DOE contractors from
U.S. Department of Energy
Office of Scientific and Technical Information
P.O. Box 62
Oak Ridge, TN 37831

Telephone: (865) 576-8401
Facsimile: (865) 576-5728
E-Mail: reports@adonis.osti.gov
Online ordering: http://www.osti.gov/bridge

Available to the public from
U.S. Department of Commerce
National Technical Information Service
5285 Port Royal Rd.
Springfield, VA 22161

Telephone: (800) 553-6847
Facsimile: (703) 605-6900
E-Mail: orders@ntis.fedworld.gov
Online order: http://www.ntis.gov/help/ordermethods.asp?loc=7-4-0#online

SAND2008-1333
Unlimited Release
Printed February 2008

Final LDRD Report: Infrared Detection and Power Generation Using Self-Assembled Quantum Dots

Jeffrey G. Cederberg
Advanced Materials Sciences

Eric A. Shaner
Semiconductor Material and Device Sciences

Robert Ellis
Applied Photonic Microsystems

Sandia National Laboratories
P.O. Box 5800
Albuquerque, New Mexico 87185-1086

ABSTRACT

Alternative solutions are desired for mid-wavelength and long-wavelength infrared radiation detection and imaging arrays. We have investigated quantum dot infrared photodetectors (QDIPs) as a possible solution for long-wavelength infrared (8 to 12 μm) radiation sensing. This document provides a summary for work done under the LDRD "Infrared Detection and Power Generation Using Self-Assembled Quantum Dots". Under this LDRD, we have developed QDIP sensors and made efforts to improve these devices. While the sensors fabricated show good responsivity at 80 K, their detectivity is limited by high noise current. Following efforts concentrated on how to reduce or eliminate this problem, but with no clear path was identified to the desired performance improvements.

CONTENTS

LIST OF FIGURES

LIST OF TABLES

1. BACKGROUND AND SCOPE

1.1 Overview of Problem and Idea

Epitaxial growth has advanced to a level that enables atomic layer control of semiconductor materials deposition and the creation of self-assembled structures with nanometer length scales. The nanostructures known as self-assembled quantum dots, have optoelectronic properties that are not achieved in bulk or quantum well structures. Optoelectronic devices utilizing self-assembled quantum structures have shown enhanced performance over bulk and quantum well devices. A quantum dot infrared photodetectors (QDIP) is one device that exploits the characteristics of quantum dots that are not available with other semiconductor heterostructures. QDIP utilizes the electrons in the conduction band to couple to infrared radiation. Unlike quantum well infrared photodetectors (QWIP), quantum dots are sensitive to normal incidence radiation. They are also predicted to have enhanced responsivity because the longer lifetime of photoexcited carriers and lower dark current than their QWIP counterparts. This project has exploited our efforts in the material science of quantum dots to evaluate QDIP designs for the 8 to 11 μm atmospheric window, known as the long-wavelength infrared (LWIR) and demonstrate the feasibility of these devices.

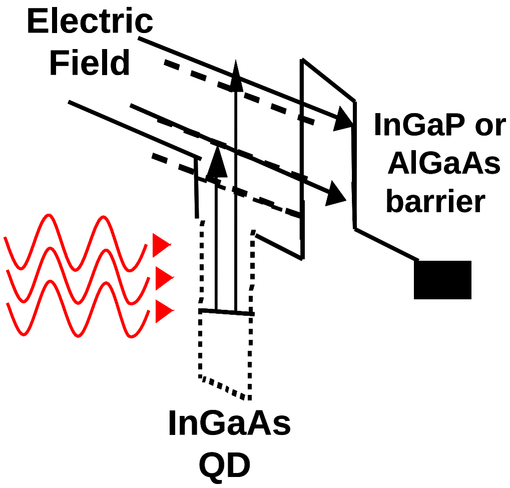

Figure 1. Conduction band diagram of a QDIP structure.

A QDIP utilizes the ground to excited state transitions in the conduction band of quantum dots to couple to the incident radiation as shown in Figure 1. The ground state is populated by extrinsic doping introduced into the structure. Electrons that are promoted to the excited state upon irradiation either achieve enough energy to escape the potential or get close enough to the top of the potential to quantum mechanically tunnel out of the barrier. The photoexcited electrons produce a current proportional to the intensity of the incident infrared radiation.

1.2 Present and Alternative Technology

LWIR detectors are dominated by two commercially available materials. HgCdTe (MCT) and GaAs/AlGaAs QWIP. MCT is the material of choice for the mid-wavelength infrared (MWIR, 3-5 µm), providing a broad wavelength response for wavelengths smaller than the cutoff wavelength and the ability to manufacture a photodiodes and detector arrays with very low dark current. In the LWIR the same technology applies, however the performance of MCT in the LWIR is not as good, having lower detectivities and higher dark current, and it requires lower operating temperatures (around 80 K). In addition, MCT is a notoriously difficult material to fabricate on a large scale, although significant progress has been made through painstaking development. Even with these fabrication difficulties large 1024 x 1024 pixel FPA using MCT are available. GaAs/AlGaAs QWIP devices have excellent response in the LWIR. Their fabrication leverages mature GaAs-based material growth and processing to achieve low defect density structures resulting in high pixel operability. QWIPs are not without problems that make them unattractive from a systems standpoint. Quantum mechanical selection rules do not allow the QW ground state to couple to normal incidence radiation. This requires elaborate three-dimensional structures to be etched into the QWIP device to diffract the incident radiation into the plane of the device. They are photoconductive devices, with a larger required power for operation. The cooling load required for QWIPs is larger than for MCT devices at the same wavelength. This makes them less attractive for remotely operated systems. An alternative technology that has been proposed is type II superlattice of In(AsSb) and (InGa)Sb utilizing the confined hole states in InGaSb and the electron states in InAsSb. The cutoff wavelength of this device can be tuned from the MWIR through the VLWIR by changing the composition and layer thicknesses in the structure. This technology involves homoepitaxy on immature GaSb substrates or mismatched heteroepitaxy on GaAs, which is technologically underdeveloped. The demonstrated dark current in superlattice photodiodes is not much better than photoconducting QWIP devices at similar cutoff wavelengths and operating temperatures.

QDIPs have the potential to provide the advantages of both MCT and QWIP devices in the LWIR. QDIP devices, as with QWIPs, leverage the mature fabrication of GaAs-based devices. This means that the production is scalable to large area wafers (4 inch diameter or larger) and the defects on the wafers are have a low density allowing the potential for a high percentage of operability. These factors translate into potentially cheaper fabrication for the sensor array. They have shown detectivities comparable to MCT in the MIR at higher operating temperatures. This gain in operating temperature is due to the limited overlap of the quantum dot states with thermal carriers in the bulk of the device resulting in lower dark current. This makes them attractive from a systems standpoint that the functionality of the FPA could be increased for the same cooling load or the cooling load required by the system could be reduced. The enhanced responsivity arises from the longer lifetime of photoexcited carriers, which allows more of the photoexcited carriers to be removed from the device before relaxing to the ground state. In addition, QDIPs provide a route to multispectral sensing using the applied voltage to tune the response wavelength from the LWIR into the MWIR. It might be possible to get 10 μm response at one voltage and a 5 μm response at another.

1.3 Scope of Report

Chapter 1 has motivated why QDIPs are of interest to Sandia National Laboratories and the position they may fill in our technology portfolio. Chapter 2 will provide an assessment of QDIP technology. Section 2.1 is a quantitative literature review about what has been done and reported by others working on this technology. Section 2.2 concentrates on modeling of QDIP performance to understand how this technology can be improved. This section compares the results of the model to the available literature results and identifies areas were QDIP may have an impact.

Chapter 3 focuses on the results obtain under this LDRD. Section 3.1 discusses QDIP design and fabrication. Section 3.2 presents initial device results and discusses the challenges that they brought about. Chapter 4 summarizes the efforts made to improve QDIP performance. Section 4.1 discusses the results associated with extending the active region thickness to increase the quantum efficiency of the QDIP. Section 4.32 describes our efforts to improve quantum dot uniformity and size distribution. Finally Chapter 5 will summarize our efforts with conclusions drawn from the work performed.

2. TECHNOLOGY ASSESSMENT

2.1 Literature Review

Extensive work on QDIP technology has been performed prior to Sandia's entry into this technology. A quantitative review of previous reported performance was performed in order to be aware of the current state-of-the-art. The Table 1 below summarizes this effort. As with any technology, QDIPs have matured over the three years during this LDRD in terms of increasing the detectivity and increasing the range of operating temperatures. This is encouraging, suggesting that QDIPs may find a path to a commercial product. The structures have advanced from repeated layers of self-assembled quantum dots in a GaAs or AlGaAs matrix. High performance structures typically use the quantum dot to fix the ground state energy while excited states are determined by the materials around the quantum dot. The dimensions of these encapsulation layers provide a critical degree of freedom for QDIP design. A significant number of III-V materials have been used to design QDIP structures. The control required for QDIP fabrication means that only two techniques are feasible. QDIP fabrication is dominated by molecular beam epitaxy (MBE), but several high performance structrues have been obtained with metal-organic chemical vapor deposition (MOCVD).

Table 1. Literature review of QDIP performance

Reference (Location)	Material System (technique)	λ_C [µm]	D^* [cm $Hz^{1/2}$/W]	R_λ [A/W]	J_{dark} [A/cm^2]	Δλ/λ [%]	Max T [K]
Appl. Phys. Lett., **91**, 051115, (2007) (U of Mass. – Lowell)	InAs QD with $In_{0.2}Ga_{0.8}As$ cap (MBE)	9.9	1.1E8 @ 190 K, 0.25 V	2.5 @ 190 K, 0.25 V		0.2	190
Appl. Phys. Lett., **90**, 131112, (2007) (Northwestern)	InAs QD with InGaAs cap in InAlAs on InP (MOCVD)	4	2.8E11 @ 120 K, -5V	0.6 @ 120 K, -5V	5E-6 @ 120 K, -5V	13	220
Appl. Phys. Lett., **86**, 191103, (2005) (Northwestern)	InAs QD with InGaAs cap in InAlAs on InP (MOCVD)	6.5	2E9 @ 100 K, 1 V	0.004 @ 100 K, 1 V	6.2e-5 @ 100 K, 1 V	12	100
Appl. Phys. Lett., **91**, 173508, (2007) (Australian National University)	$In_{0.5}Ga_{0.5}As$ QD in AlGaAs	7	3E9 @ 77 K, 0.5 V	0.04 @ 77 K, 0.5 V		20	77
Appl. Phys. Lett., **91**, 013503, (2007) (U. of Sheffield, UK)	InAs QD with $In_{0.15}Ga_{0.85}As$ DWELL (MBE)	7.5	5E10 @ 77K and -2 V	1 @ 77K and -2 V		20	110
Appl. Phys. Lett., **91**, 143502, (2007) (U. of Sheffield, UK)	InAs QD with $In_{0.15}Ga_{0.85}As$ DWELL (MBE)	8 to 11.6	1E10 @ 77 K and -2 V	0.1@ -2 V, 77K	2E-4 @ 77K, -2 V	12	77 K
J. Vac. Sci. Technology, B**24**, 1553, (2006) (U. of New Mexico)	InAs QD with $In_{0.15}Ga_{0.85}As$ DWELL (MBE)	9.7	4e10 @ 77 K and ±1.5 V		1E-9 @ 77 K, ±1.0V	23	77 K
Appl. Phys. Lett., **86**, 191106, (2005) (U. of Michigan)	$In_{0.6}Ga_{0.4}As$ QD with GaAs/AlGaAs barrier (MBE)	6	2.4E10 @ 77K, 2 V	0.7 @ 80 K, 4 V	0.5 @ 300 K, 1 V	12.5	80
		17	1.5E7 @ 300 K, 1 V	0.15 @ 300 K, 2 V		41	300
J. Appl. Physics, **99**, 114517, (2006) (Australian National University)	$In_{0.5}Ga_{0.5}As$ QD in GaAs	6.2	1.6E9 @ 77K, 1.3 V	0.007 @ 77 K, -1.3 V,	1E-3 @ 77 K, -2 V	22	77
Appl. Phys. Lett., **82**, 1986, (2003) (U. of Florida)	$In_{0.6}Ga_{0.4}As$ QD (MBE)	7.6	1.1E10 @ 77K, -2 V	0.22 @ 77K, -2 V	2.5E-04 @ 77K, -2 V	17.1	260

Source (Location)	Material System (technique)	λ_C [µm]	D^* [cm Hz$^{1/2}$/W]	R_λ [A/W]	I_{dark} [A/cm^2]	$\Delta\lambda/\lambda$ [%]	Max T [K]
Electrons Letters, **38**, 1374, (2002) (U. of Florida)	InAs QD with InGaP cap (MBE)	12.2	3.4E9 @ 77K, -1.7 V	0.05 @ 77 K, 1.7 V	1E-6 @ 77 K, 1.7 V	22	77
Appl. Phys. Lett., **84**, 3277, (2004) (USC and UT-Austin)	InAs with InGaAs SRL cap (MBE)	8.7	3E11 @ 78K, 1.4 V	0.71 @ 78K, 1.4 V	4.9E-04 @ 78K, 1.4 V	10	100
Appl. Phys. Lett., **81**, 1369, (2002) (U. of New Mexico)	InAs DWELL/GaAs (MBE)	7.2	2E9 @ 1 V, 78 K	3.6 @ 1 V, 78 K	0.2 @ 1 V, 78 K	35	85
J. Appl. Physics, **92**, 7462, (2002) (USC and UT-Austin)	InAs with InGaAs SRL in GaAs (MBE)	8.8	3.2E9 @ -0.1 V, 77 K	0.66 @ -0.1 V, 77 K	1 @ -0.1 V, 77 K	12	120
J. Appl. Physics, **82**, 2574, (2003) (U. of New Mexico)	InAs DWELL/GaAs (MBE)	4.2	1.5e9 @ -1V, 60 K	0.1 @ -1V, 60 K	1.00E-05 @ -1V, 60 K	100	91
		7.6				46	
J. Appl. Physics, **92**, 4141, (2002) (USC and UT-Austin)	InAs with InGaAs SRL in GaAs (MBE)	5.5	3.7E9 @ 77K, 0.3 V	0.1 @ 77K, 0.3 V	0.1@ 77K, 0.3 V	12	100
		8.9	7.3E8 @ 77 K 0.8V	0.5 @1V		12	
Appl. Phys. Lett., **84**, 2166, (2004) (Northwestern)	InGaAs/InGaP (MOCVD)	4.7	3.6E10 @ -1.6 V, 95 K	3.1 @ -1.6 V, 95 K	6.25E-09 @ -1.6 V, 95 K	14	140
J. Appl. Physics, **96**, 1036, (2004) (U. of New Mexico)	InAs DWELL/GaAs (MBE)	7.5	5.1E9 @ -0.8 V, 60 K	0.105 @ -0.8 V, 60 K	3.90E-06 @ -0.8 V, 60 K		
IEEE Photonics Technology Letters, **16**, 1361, (2004) (U. of Michigan)	InAs/GaAs (MBE)	4.9	2E10 @ 2 V, 175 K	0.12 @ 2 V, 175 K	1.00E-04 @ 2 V, 175 K	~0.2	200

Source (Location)	Material System (technique)	λ_C [µm]	D^* [cm Hz$^{1/2}$/W]	R_λ [A/W]	I_{dark} [A/cm^2]	$\Delta\lambda/\lambda$ [%]	Max T [K]
Appl. Phys. Lett., 75, 2719, (1999) (U. of Virgina)	$In_{0.3}Ga_{0.7}As$/ GaAs (MBE)	10.2	7E9 @ 40K, 0.4 V	0.023 @ 30 K, 0.4 V		10	40
Appl. Phys. Lett., **85**, 4154, (2004) (Stanford)	InGaAs/InGaP (MOCVD)	5.5	4.7E9 @ 77K, -2 V	2.2 @ 77K, -4 V			77
Appl. Phys. Lett., **88**, 153109, (2006) (Carnegie Mellon)	InAs QD in GaAs (MBE)	9.2	7.2E8 @ -0.8 V	0.14 @ -0.8 V,	2E-3, 100 K, 5 V	50	220
		5	2E9, @ 2 V, 100 K	4 @ 100 K, 5 V			
J. Vac. Sci. Technology, **B23**, (2005), 1132 (Carnegie Mellon)	InAs QD in GaAs (MBE)	5	1E7 @ 78 K, 0.6 V	0.014 @ 77 K, 0.6 V	0.01 @ 78 K, 0.2 V	44	78

2.2 Modeling QDIP Performance

MCT is an established technology for optical sensors in MWIR (3-7 µm) and LWIR (7 – 13 µm) spectral regions. However this technology is not without detractions related to growth and processing issues: low yields and variable processing resulting in high cost. An alternative technology is QDIP sensors based on self-assembled quantum dots based on III-V semiconductors. The quantum dots are formed through the strain energy driven 2D to 3D morphology transition when compressively strained films (InAs or InGaAs) are grown on larger bandgap matrices (GaAs, AlGaAs, or InGaP). The conduction band potentials are populated with electrons from intentional doping. Photons of the appropriate wavelength can promote an electron from the ground state to an excited or continuum state. QDIP devices have been the subject of intense interest as a possible replacement for MCT and as a possible route to VLWIR sensors [1]. The development of QDIP sensors could then leverage the developed focal plane array (FPA) technology for quantum well infrared photodetector (QWIP) FPAs. This paper compares a subset of the existing data for MCT and QDIP devices. The data for MCT has been provided from FPA devices obtained from Jeffrey Rienstra and the data for QDIP has been gathered from single pixel devices reported in the literature. Two models are considered for QDIP devices. The first considers only quantum dots with a uniform size, with no variation in size or resulting energy levels [2,3]. The second considers the inhomogeneous broadening of quantum dot energy levels [4]. The second model has been utilized to consider the impact of structure modifications for the QDIP that could improve performance to meet or exceed that of MCT sensors.

The figure of merit (FOM) that was selected for comparison is peak absorbance/dark current density. For ease calculation this comparison utilizes the peak responsivity (units of A/W) in place the peak absorbance since both quantities are proportional to the joint density of states. The other issue in comparison is the fact that QDIP devices are photoconductive, while MCT devices are photovoltaic. Photoconductors can exhibit gain that can enhance the responsivity. No attempt has been made to remove this from the data presented. For the calculated FOM values the gain has been set to unity to provide a direct comparison to MCT devices.

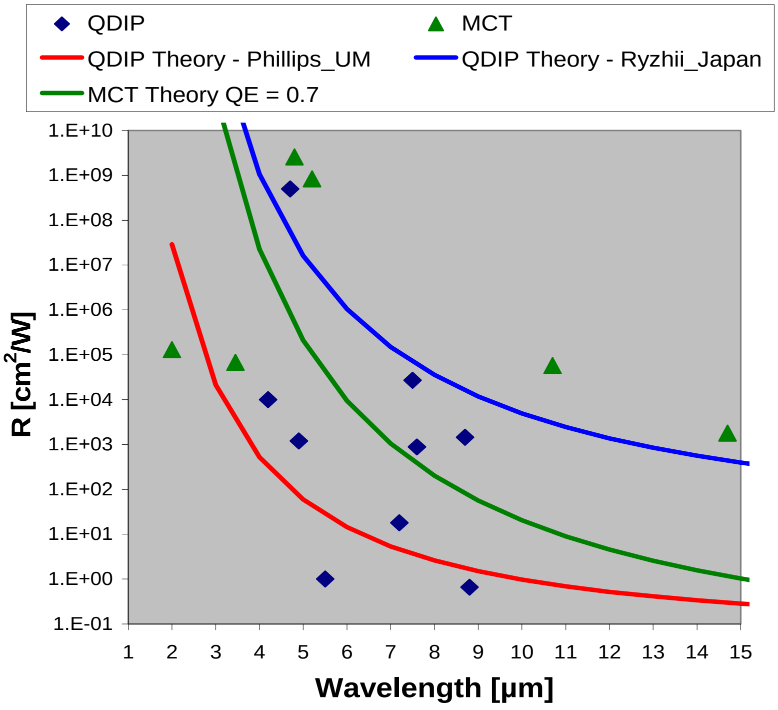

Figure 2. Modeled FOM for QDIP and the reduced FOM from the literature review performed.

The figure above shows the complied FOM data for MCT and QDIP. The MCT data were generated under several assumptions. The responsivity values are generated from the external quantum efficiency, η, (EQE) and the cutoff wavelength (λ) through the relationship: R = qη (λ/hc), where other symbols have their usually meanings. The dark current, J_{dark}, was evaluated from measured R_0A to calculate the diode saturation current, which is a lower limit on the dark current in reverse bias, through the relationship $J_s = (qR_0A/kT)^{-1}$. The responsivity and dark current density data for QDIP were taken directly from publications and converted to the FOM. In general MCT values are higher than QDIP results by several orders of magnitude; however, several demonstrations suggest that QDIP structures can come close to the performance of MCT.

The green curve assumes a constant EQE of 70% to evaluate the responsivity for MCT. The model for the dark current density is the thermal generation rate in the region defined by the absorption length (1/α), as developed by Kinch [5]. The dark current model clearly over estimates the current by several orders of magnitude, resulting in the lower theoretical FOM. 150 K was used for this calculation.

The blue curve utilizes the model developed by Ryzhii, et al.[2,3] for QDIP. This model considers the band structure of ideal quantum dots with no energy level distribution, but it does allow a number of structural parameters to be investigated: the QD density, number of periods, and others. There are a large number of assumed or estimated parameters in this model that make accurate evaluation questionable at this early stage, making the prediction of performance matching or exceeding MCT sensors tentative at best.

The red curve utilizes the model developed by Phillips, which extends the work of Kinch [5]. This model develops a theoretical expression for the absorbance of a layer of QD, which considers similar parameters as Ryzhii and includes the inhomogeneous broadening of the QD ensemble. The curve shown assumes an ensemble that is 50 times broader than the emission from a single QD, which is on the high side of presently available technology. This model seems somewhat pessimistic, given that almost all of the experimental results presented exceed this theoretical estimate. It should be noted that both QDIP model curves assume only 10 periods of QD with an aerial density of 5×10^{10} cm^{-2} operating at a temperature of 150 K.

Since QDIP sensors are performing below that of MCT the obvious question is what parameters can be changed to improve the QDIP FOM. The obvious parameter is the number of QD layers. Table 2 shows the FOM for 10, 20, and 50 QD layers with a fixed inhomogeneous broadening ratio of 50 at wavelengths of 5 and 10 µm, a temperature of 150 K, and a QD density of 5×10^{10} cm^{-2}.

Table 2. Figure of Merit (FOM) for different numbers of periods in active region.

Number of QD layers	FOM (R/J_{dark}) for 5 µm [cm^2/W]	FOM (R/J_{dark}) for 10 µm [cm^2/W]
10	59	1
20	119	2
50	296	5

All of these predicted FOM for QDIP devices are several orders of magnitude below the experimental data for MCT. The density of QD is near saturation (fill factor of 0.45). Increasing the QD density to 1 x 10^{11} cm^{-2} (fill factor of 0.63) will increase the FOM to 1540 cm^2/W at 5 µm and 20 cm^2/W at 10 µm. The question that would arise through utilizing this design parameter is if the QDs with 0.63 fill factor have the same band structure as ones grown at the lower 0.45 fill factor.

The inhomogeneous broadening of QD can be reduced from the value of 50 to as low as 20, causing the FOM to increase to 148 cm^2/W at 5 µm and 2 cm^2/W at 10 µm for 10 QD layers with a QD density of 5 x 10^{10} cm^{-2}. If all the above improvements were made to the QDIP structure a FOM of 1.8 x 10^6 cm^2/W at 5 µm and 250 cm^2/W at 10 µm. Both of these idealized FOM fall short of the experimental values for MCT.

A spectral region that might be difficult to fill for MCT is the VLWIR band (15 µm and beyond) that is presently filled by extrinsic detectors (doped Si or Ge) operating a liquid He temperatures (2-10 K) and bolometers. QDIP sensors operating on a bound to bound intersubband transition might be able to raise the operating temperature to that of liquid N_2 and possibly to 150 K. The Table 3 considers the predicted FOM for MCT and QDIP at 20 µm for a temperature of 150 K. Two QDIP structures are provided: the structure available at present (5 x

10^{10} cm^{-2}, 10 layers, inhomogeneous broadening of 50) and the idealized structure (1 x 10^{11} cm^{-2}, 50 layers, inhomogeneous broadening of 20).

Table 3. FOM for MCT in comparison to current QDIP technology and ideal QDIP technology for VLWIR operation

Material	FOM (R/J_{dark}) for 20 µm [cm^2/W]
MCT	0.2
Present QDIP	0.2
Idealized QDIP	4.5

The present QDIP might be able to meet the performance of MCT with the presently available technology and should be able to perform significantly better if modest improvements can be achieved.

2.3 Summary

The relevant literature associated with QDIPs has been review, documenting the performance to the date of this publication. Continuous improvement by the researchers working on these structures has been made suggesting that QDIPs might find be incorporated into a commercial system in the future. Two models of QDIP performance have been implemented. Both of these models suggest that QDIPs will have difficulties achieving the performance already available with MCT in the MIR or LWIR. QDIPs may be competitive to MCT in the VLWIR.

3. QDIP DESIGN AND PERFORMANCE

3.1 QDIP Design

To obtain the performance enhancements that are predicted from our modeling requires design that can be extended to arbitrarily thick QDIP-active regions. We developed the idea to look at strain balanced QDIPs as depicted in Table 4. The goal is to reduced the strain energy of each period of quantum dots to zero. In practice there are is some strain introduced due to the fact that exact compensation is not possible. MOCVD has the capability to easily incorporate phosphorous into GaAs to form GaAsP alloys that are in tension with respect to the GaAs substrate they are grown on. GaAsP can compensate for the compressive stress introduced by the array of InAs quantum dots and InGaAs layer used to cap the quantum dots. The desirable characteristic of this design is that the InGaAs cap acts as a quantum well

Table 4. Strain compensated QDIP design.

Repeated	Layer	Thickness [nm]	Doping [x 1E18 cm^{-3}]
No	GaAs	200	2
No	GaAs	50	NID
Yes	GaAs	26	NID
Yes	$GaAs_{0.95}P_{0.05}$	24	NID
Yes	$In_{0.10}Ga_{0.90}As$	6	NID
Yes	InAs QD	0.6	2
No	GaAs	50	NID
No	GaAs	500	2
No	AlAs	50	NID
	GaAs substrate		Semi-insulating

superimposed on the ground state of the quantum dot and allows the excited state to be determined by varying the thickness of the capping layer. If the GaAsP strain compensation layer were not present the strain energy of the QDIP stack would increase for each layer put down, eventually causing dislocations to be introduced. The effect of GaAsP on the InAs quantum dots is not know. Since the quantum dots are also compressively strained GaAsP can act in opposition to their strain field. However, this strain field is highly localized and cannot be compensated for efficiently.

3.2 QDIP Fabrication

All the QDIPs investigated during this project were grown by low pressure MOCVD at 70 Torr. Triethyl gallium (TEGa), trimethyl indium (TMIn), and trimethyl aluminum (TMAl) were the group III metal-organic sources used. Arsine ($AsH_{3)}$ and phosphine (PH_3) hydride sources supplied group V elements. A mixture of 30 ppm disilane (Si_2H_6) in hydrogen was used for n-type doping of the quantum dots and the contact layers of the structure in Table 4. Nominal singular GaAs(100) was used for all growths. This provides the smooth starting surface needed for quantum dot growth. After a thin GaAs buffer, 50 nm of AlAs was grown as an etch stop to help fabrication of the mesa pixels. The bottom GaAs contact layer was then grown followed by a 50 nm undoped GaAs layer, both grown at 600°C. The InAs layer that forms the quantum dots was then grown at 480°C. After a 10 second pause in the growth to allow the InAs layer to transition to quantum dots, the quantum dots were capped with 6 nm of $In_{0.1}Ga_{0.9}As$. The temperature was then ramped back to 600°C for growth of the 24 nm $GaAs_{0.05}P_{0.95}$ layer and the remaining 26 nm GaAs layer. This allows the cycle to repeat to form the active layer of the QDIP.

The conversion of the planar epitaxial structure into QDIP pixels is a simple process. Mesas are defined using Shipley 4330 photoresist and lithography. The photoresist acts as a mask and the mesas are etched into the film down to the bottom contact layer using a 500 W inductively couple plasma (ICP) reactive ion etch (RIE) formed with BCl_3 and Ar at 3 mTorr. The photoresist mask is removed and a second lithograph step defines open areas for contact metal to be deposited. The metallization for both contacts is formed in a single step. A metal stack of Ni/Ge/Au/Ni/Au (8/27/54/14/150 nm) is deposited by electron beam deposition. After the deposition the photoresist mask is lifted-off in acetone. The final processing step is to anneal the metal stack to insure low contact resistance to the underlying semiconductor. This is performed in a rapid thermal process furnace at 400°C for 30 sec at atmospheric pressure in an argon ambient. A microscope image a completed pixel is shown inset in Figure 3.

Before the pixels can be measured they need to be mounted into a gold-plated copper package. This allows wire bonding of the metal pads to the package. For measurement the package is then mounted in a closed-cycle He cryostat for measurement at variable temperatures between room and 20 K. The field of view of the cryostat is 33° relative to the sample normal. Spectral measurements were performed using a Nicolet 670 Fourier-transform infrared (FTIR) spectrometer. The uncalibrated signal from the QDIP under test is detected by a Keithley 428 preamplifier. Calibrated measurements were made using a black-body source for excitation. Noise current measurements necessary for determining the detectivity of the device were performed with a SR770 fast Fourier transform analyzer.

3.3 Experimental QDIP Performance

Initial QDIP single pixels showed performance up to 50 K. The design presented in Section 3.1 was able to extend the operating temperature to 80 K as shown in Figure 3. In addition to the improved operating temperature, the QDIP showed a primary transition at 8 µm, which is shorter than the targeted wavelength of 10 µm. This suggest that the 6 nm $In_{0.1}Ga_{0.9}As$ layer of the QDIP is not thick enough to lower the excited state energy. However, this shows the ease in which the QDIP design can be modified to be sensitive to any transitions. An additional transition around 12 µm is observed at positive bias showing the asymmetry of the QDIP transitions and the possibility to have two-color, voltage-tunable detection. Calibrated measurements were made for these devices. Figure 4 shows the peak responsivity and peak detectivity as a function of bias voltage is shown in Figure 1. Our design achieved 0.5 A/W at 80 K and 4.6 V, which is quite good

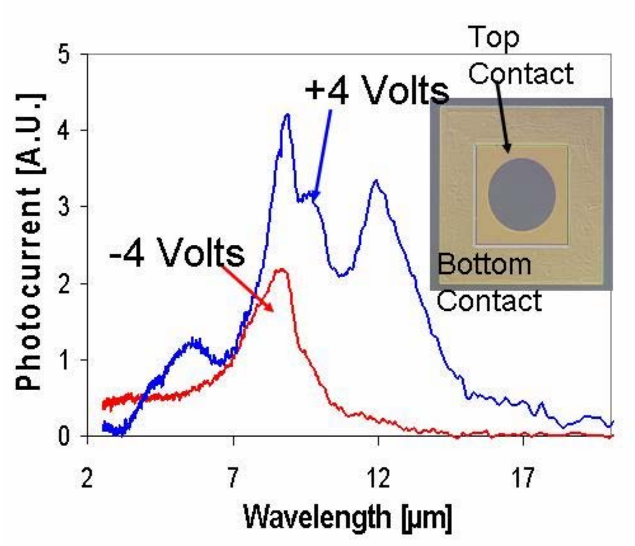

Figure 3. Photocurrent spectrum of initial device measured at 80 K. Inset shows plan view of single pixel device.

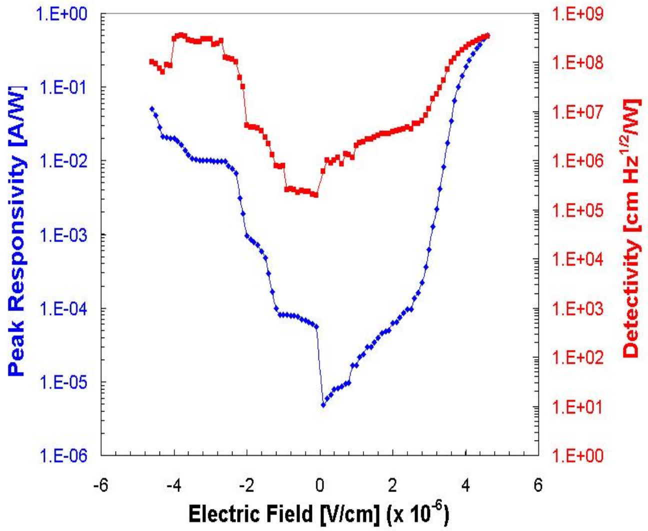

Figure 4. Responsivity and detectivity as a function of electric field for an initial QDIP detector. All measurements made at 80 K.

static performance as shown by a comparision to Table 1. We speculated as part of the original proposal that increased responsivity might be achieved by making the active layer thicker by growing more periods of quantum dots with the associated cap and strain balancing layer. The peak dynamic detectivity is limited by high dark current to 3 x 10^8 cm $Hz^{1/2}$/W at 80 K and 4.6 V. The possibility of having high dark currents in our devices was discussed as part of the original proposal.

Several issues could impact the dark and noise current of the QDIP. The quantum dots in the design developed are doped with silicon donors directly. Unoptimized doping may produce too many free carriers in the quantum dot, effectively overfilling it. Under small bias these electrons spill out and contribute to the thermal dark current and the noise current under operation. Another possibility is that the interaction of the dopant atoms directly with the InAs quantum dot. This has been reported by others, but we have not observed any structural degradation of the quantum dots by direct doping. On possibility to avoid direct doping of the quantum dots is to dope the GaAs or GaAsP barrier materials. This introduces difficulties with the design as now the carrier density in the quantum dot is not a function of the amount of dopant introduced, but rather the separation of the dopant sheet from the quantum dot layer. This approach was not investigated in our effort. Finally, we proposed that large, relaxed quantum dots could act as electrical shunts. These over-grown quantum dots could contribute to the abnormally high dark current, but would not limit the responsivity of the detector. Further efforts concentrated on understanding how to limit large quantum dot formation during growth.

4. EFFORTS TO IMPROVE QDIP PERFORMANCE

4.1 Active region thickness

QDIPs are limited by their quantum efficiency. A single layer of quantum dots converts less than 1 percent of the incident photons into electrons. One way to improve the quantum efficiency is to increase the number of layers of quantum dots in the active layer of the QDIP. It was believed that an increased number of quantum dot layers would result in an increase in the responsivity of the device. The problem with strained structures, such as the QDIP, is that each layer of quantum dots introduced increases strain energy of the active layer and the increases the opportunity for structural defects to be introduced. This fact motivated us to investigate a strain balanced design so that the improvements predicted by larger active layer thicknesses could be achieved.

To investigate our hypothesis that thicker active layers should provide more quantum efficiency, two structures were grown. One had 10 periods of InAs quantum dots while another had 20 periods. Both structures were determined to be strain balanced based on x-ray diffraction rocking curves. Both structures showed strong photoluminescence, however the thicker structure did not show a factor

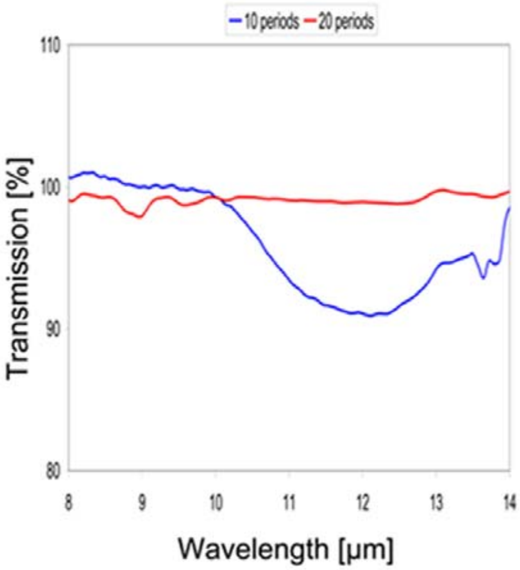

Figure 5. Transmission through 10- and 20-period QDIP structures performed at 77 K.

of two increase in the photoluminescence intensity. Instead of fabricating these structures into QDIPs, IR transmission measurements were performed at 77 K to determine if any features attributable to intrasubband transitions of quantum dot could be observed. Figure 5 shows the data obtained. A clear transition is observed between 10 and 13 μm for the 10-period structure. No transitions are observed for the 20-period structure, suggesting that by increasing the active layer thickness we have degraded the desirable properties of the quantum dot.

4.2 Quantum Dot Uniformity

One source of dark current in QDIPs is large, relaxed quantum dots. These structures act as vertical shunt paths for current through the device. In an effort to improve QDIP performance we looked at the size distribution of the quantum dots that were formed under different conditions. Experimental island count histograms as a function of quantum dot volume have been evaluated using an established model. The experimental data was obtained for 2 inch and analyzed over the center 26 x 26 mm square of the wafer with atomic force microscopy. More than one distribution is required for all conditions investigated to obtain adequate representations of the experimental data. Consistent parameters are obtained for samples grown with a variable InAs thickness. Higher growth temperatures results in material being converted into relaxed islands. Extended annealing without AsH_3 eliminates small islands, suggesting that they are not a stable distribution.

InGaAs self-assembled quantum dots have been studied extensively over the past 15 years addressing fundamental questions related to their three-dimensional quantum confinement and a variety of applications. Initial research of InGaAs-based quantum dots was motivated by the possibility of achieving active regions that emit at 1.3 or 1.55 μm to replace and improve upon InP-based quantum well devices.[6, 7, 8] Quantum dots discrete characteristics naturally lead into applications utilizing them for single photon detectors.[9] Quantum dots have been utilized to demonstrate middle infrared detectors [10,11], which is our primary interest.

The optimization of InGaAs quantum dots on GaAs (100) has been largely an empirical effort. Basic phenomenological models have provided insight into quantum dot formation and development as of function of growth parameters.[12, 13, 14] This can be contrasted to the even more widely studied Ge(Si) on Si (100) system, where extensive fundamental modeling has been undertaken.[15] There is a need for quantitative modeling addressing experimentally determined quantum dot size distributions in the InAs/GaAs (100) material system.

A general thermodynamic model for quantum dot size distributions was first posed by Shchukin, *et al*.[16] With this model they evaluated the stability of quantum dots with respect to ripening. They determined the importance of the surface energy and the dipole interaction energy to distribution stabilization and determined regions where distributions would be stable and unstable. Daruka and Barbási extended this model providing a phase plot of the different regimes of island formation as a function of strain and deposit thickness.[17] More recently Rudd, *et al.* has combined the previous developments into a tractable model that allows fitting experimental histograms of island count versus island size.[18] They applied their model to fitting Ge on Si (100) where the pyramid to dome transition produces bimodal distributions that vary with the growth temperature and Ge thickness deposited. We utilizes the thermodynamic model as developed by Rudd, *et al.* and apply it to the InAs on GaAs (100) system. An overview of the derivation leading to development is provided. The conditions relating to sample formation are given and the details of how the histograms are generated from extensive atomic force microscopy (AFM) images. The histograms and their fits are compared for a variety of conditions.

4.2.1 Model Development

Since the system under consideration is open and isothermal we use the grand canonical ensemble to describe island evolution. The partition function of interest is given as:

$$\Xi = \sum_{configurations} e^{-(E_{total} - N\mu)\beta} \tag{1}$$

Ξ is the grand partition function for an open system exchanging material and energy with its surroundings. β represents $1/kT$, where T is the absolute temperature of the system, and k is Boltzmann’s constant, and μ is the chemical potential of the InAs film. E_{total} is the total internal energy of the ensemble and can be expressed as:

$$E_{total} = \sum_{v} nE_v \tag{2}$$

Where n is the number of islands containing v atoms and E_v is the energy of an island with size v. N is the total number of atoms in all islands and can be expressed as:

$$N = \sum_{v} vn \tag{3}$$

Substituting (2) and (3) into (1) and converting the sum over configurations to a sum over the number of molecules gives:

$$\Xi = \sum_{n} \frac{e^{-\sum_{v} n(E_v - v\mu)\beta}}{n!} = \sum_{n} \frac{\prod_{v} e^{-n(E_v - v\mu)\beta}}{n!} \tag{4}$$

The factorial denominator results from the conversion of the sum over configurations to the sum over states. Ensemble averages for the island size $<n>$ are expressed as:

$$< n >= \frac{\sum_{n}\prod_{v} e^{-n(E_v - v\mu)\beta}\frac{n}{n!}}{\sum_{n}\prod_{v}\frac{e^{-n(E_v - v\mu)\beta}}{n!}} = \frac{\prod_{v}\sum_{n} e^{-n(E_v - v\mu)\beta}\frac{n}{n!}}{\prod_{v}\sum_{n}\frac{e^{-n(E_v - v\mu)\beta}}{n!}} = e^{-(E_v - v\mu)\beta} \tag{5}$$

The energy of an individual island containing v molecules can be expressed as:

$$E_v = (Av + Bv^{2/3} + Cv^{1/3} + D) + (2\lambda\xi^2 v^{2/3}\theta) \tag{6}$$

The coefficients associated with (6) require explanation. In the first term, *A* represents the elastic energy of the island. It is interpreted in this work as the additional energy the island has due to strain relative to the bulk film. *B* incorporates surface physics such as the reconstruction and the surface energy. *C* introduces edge effects of the island and the surface stress. A more rigorous expression for the edge energy might include an additional logarithmic term to multiply the term included here, but this is neglected in this development to simplify fitting. The volume independent term *D* can be considered as the strain energy of the wetting layer relative to the island distribution. The second term incorporates the energy dipole between islands. The elastic coefficient is represented by λ, ξ is the elastic strain dipole energy of the island, and θ is the thickness deposited. The mathematical expression used for the dipole energy is open to debate, but must be considered for dense ensembles.

The procedure adopted to fit equation (5) and (6) to a distribution of islands involves performing a minimization of the sum of squared differences between the experimentally determined island count for a specific island volume and the calculated number of islands. Island volume was used as the dependent parameter, because it can be calculated from measured data and doesn't require the atomic density of the material to be known. The minimization of the sum of squared differences was performed using the *Solver* routine in *Excel* allowing as many as five variable coefficients for each distribution. Since both *A* and μ vary with *v*, only the difference between these coefficients was evaluated. Due to the uncertainty introduced by alloying of the InAs with the GaAs substrate, no effort was made to separate λ and ξ. The temperature and material coverage are both treated as known, fixed parameters. A check was performed after a fit is obtained to see how close the calculated coverage based on $\theta = \Sigma_v(v<n>)$

was to the experimental coverage. This was used along with the sum of squared differences was used to judge the quality of the fit. Since the distributions obtained experimentally showed more than a single island type, two or more distributions are summed together with different coefficients for each distribution. This gives rises to as many as 15 variable coefficients to describe the experimental data.

4.2.2 Experimental details

The InAs quantum dots evaluated were deposited by MOCVD. The surface quantum dot samples considered were grown on top of an GaAs/AlGaAs heterostructure containing buried quantum dots. The thickness separating the buried quantum dots from those of the surface was such that the buried layer should not impact the surface quantum dots. The growth sequence follows closely a previously published procedure.[19] A post-growth purge without AsH_3 was introduced after InAs deposition to all quantum dot layers. Two temperatures were considered for InAs quantum dot formation: 480°C and 500°C. At 480°C the thickness of InAs deposited was varied: 5.4 Å, 6.0 Å, and 6.6 Å, with a constant post-growth purge without AsH_3 of 10 seconds after deposition. At 500°C the InAs thickness was fixed at 6.0 Å and the post-growth purge time without AsH_3 varied:10 seconds and 60 seconds. These two sample sets allows assessment of coefficients generated by the model to determine if they are consistent when experimental conditions are held constant.

The quantum dot density and height were measured using AFM. Imaging was performed under ambient conditions with commercial pyramidal Si tips in tapping mode. Each specimen was analyzed by taking measurements at an array of 81 points, which covered the central 26 x 26 mm^2 region of the wafer. The corners of the array are 7 mm from the wafer edge, and the centers of the array sides are 12.4 mm from the wafer edge. A scan size of 9 µm^2 was used to eliminate the effect of small-scale local variations.

The model developed uses the volume of the quantum dot as the independent variable. Experimentally, the volume cannot be determined accurately from AFM because the volume determination is subject to evaluation of island diameter. Instead we have evaluated the minimum and maximum aspect ratios, α defined as the ratio of the height to the base diameter ($\alpha \equiv h/d$), of a subset of islands as a function of their height and applied geometric formulas for a conical cap to determine island volume. The island volume was then calculated as $v = 12\pi h^3 / \alpha^2$. The aspect ratio transformation has been considered as a discontinuous first-order phase transformation, but discontinuous functions introduce mathematical difficulties into the fitting procedure. In our analysis, the dependence of the aspect ratio on island height was defined as $\alpha = \alpha_1 + \Delta\alpha \arctan(h / h_c)$. This assumes a single aspect ratio transformation of the islands consistent with our results. Larger islands relax and grow monotonically [20] which would introduce a third aspect ratio, but this observation is not implemented.

4.2.3 Results and Discussion

Figure 1a shows the island volume histogram and the associated fit obtained with the model for the sample grown at 480°C with 6.0 Å of InAs. Two distributions are required for adequate fitting of the histogram which is consistent with reports which identify a pyramid to dome transition in InAs/GaAs quantum dot.[1] Figure 1b shows the residual defined as the difference between the calculated and experimental counts. At low island volumes large absolute deviations between the fit and the data exist corresponding to about 8 percent of the experimental value. At larger island sizes the absolute fit is much better, but the percentage deviation can be as large as 16 percent.

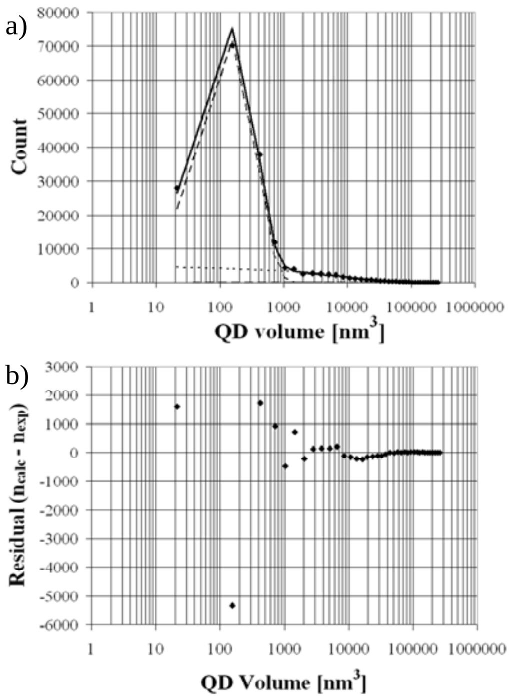

Figure 6. a) Comparison of model to experimental histogram . b) Residual, defined as the difference between the fit and experimental data.

Figure 1a can be compared to the other conditions observed for smaller and larger depositions of InAs. Figure 2a displays the histogram and its fit for 5.4 Å of InAs. Again two distributions are needed to fit the data adequately. The number of islands involved in the second distribution is lower. For the 5.4 Å sample no clear peak is observed for the first distribution, instead a broad shoulder is observed. When 6.6 Å of InAs is deposited (Figure 2b) for quantum dot formation the number of islands in the first distribution decreases and the number of islands associated with the second distribution increases. The validity of the model requires a quantitative comparison of the model parameters for constant conditions where one of the model variables is changed. In our case the sample thickness was varied. Table 5 summarizes the coefficients obtained for fits displayed in Figures 6 and 7. Analysis of the results concluded that $\lambda_2\xi^2$ needed to be fixed at a value of zero. This is physically realistic because the large islands have a low enough density that they do not interact elastically as the smaller, denser islands do. In addition to the coefficients obtained, calculated planar thickness of InAs that makes up each distribution is given at the bottom of the table. Most of the coefficients are reproduced well, with the exception being C_2.

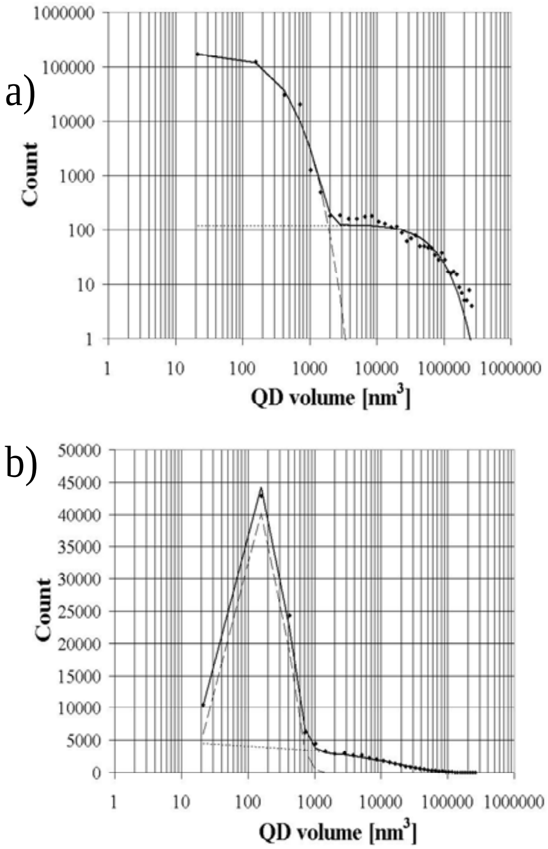

Figure 7. Experimental distributions with fits for samples grown with an InAs thickness of a) 5.4 Å and b) 6.6 Å.

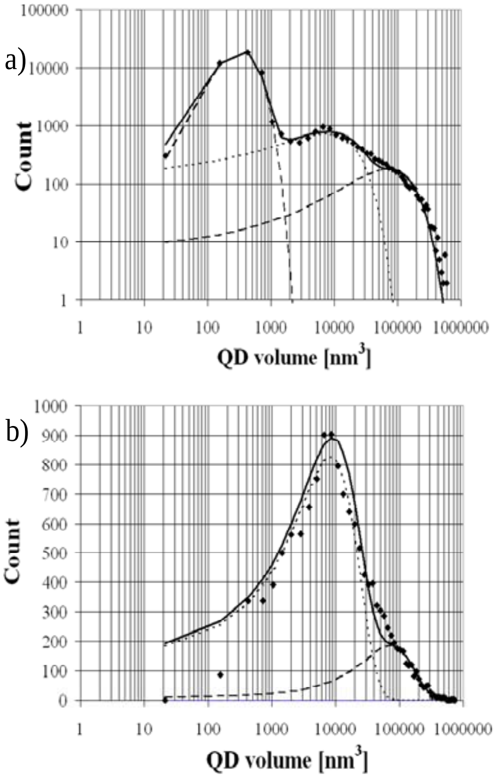

Figure 8. Experimental distributions with fits for samples grown at 500°C with a) 10 sec PGP without AsH_3 and b) 60 sec PGP without AsH_3.

Increasing the growth temperature to 500°C for a deposition of 6 Å requires a third distribution to be included to fit the data adequately. The fit obtained in shown in Figure 8a. The physical origin of the third distribution is speculated to be the strain relaxation of a significant number of the islands. Extending the purge time at 500°C to 60 seconds eliminates the first distribution as shown in Figure 8b, indicating that the small islands are unstable with respect to ripening for long anneals without AsH_3.

4.2.3 Summary

We have evaluated island count histograms as a function of volume for two MOCVD conditions using an established model. More than one distribution is required for all conditions investigated. InAs thicknesses near the critical thickness for island formation and temperatures at or below 480°C are necessary to minimize the second distribution. Consistent parameters are obtained for samples grown with variations in the InAs thickness. Higher growth temperature results in material being converted into what we propose to be relaxed islands. Extended annealing without AsH_3 eliminates small islands and leaves the distributions with larger islands unchanged, suggesting that the distribution composed of small islands is not stable for all volumes.

Table 5. Summary of parameters for the samples grown at 480°C

	T [K]	753	753	753
	θ [Å]	6.6	6.0	5.4
	AsH_3 pressure [torr]	0.27	0.27	0.27
	PGP time [seconds]	10	10	10
A_1[eV/atom]	x 10^6	-4.13	-1.24	-1.30
B_1[eV/atom$^{2/3}$]	x 10^4	-2.85	-2.91	-3.10
C_1[eV/atom$^{1/3}$]	x 10^2	-6.7	-4.7	1.6
D_1[eV]		-0.20	-0.4	-0.72
$\lambda_1\xi^2$[eV/Å/atom$^{2/3}$]	x 10^3	1.20	0.99	0.68
A_2[eV/atom]	x 10^7	1.11	1.22	1.11
B_2[eV/atom$^{2/3}$]	x 10^6	-5.72	-4.37	-7.29
C_2[eV/atom$^{1/3}$]	x 10^3	1.12	1.12	0.076
D_2[eV]		-0.55	-0.55	-0.31
θ_1 [Å]		0.3	0.45	0.67
θ_2 [Å]		6.01	4.64	0.75

5. CONCLUSIONS

QDIPs are a class of photo-conducting detectors for MWIR and LWIR radiation that may have potential applications to replace established materials, such as HgCdTe. This report has summarized our work on these optoelectronic devices. A summary of the relevant literature was performed. The progress of the community shows that continuous progress is being made on QDIP performance. Some groups have advanced their designs to the point they are fabricating focal plan arrays for imaging in the MWIR and the LWIR. The modeling performed by us suggests that QDIPs will have difficulty exceeding the continuous improvement obtained for existing technology. This is supported by the fact that experimental QDIP performance is not at the level of other more developed technologies. QDIPs still may have potential niche applications.

We were able to fabricate and test QDIP structures during this project. The QDIPs tested show good static performance, as indicated by high responsivity. However, the more relevant dynamic detectivity is limited by high thermal and noise currents. The possible origins for these current are numerous. We have investigated the possible shunting of the device by large, defected quantum dots. While we have been able to lower the fraction of these defected quantum dots, their elimination was not possible. Routes to improve QDIP performance through increasing the active thickness for IR photons to absorb could not be realized due to failure of the device as this thickness was increased.

6. REFERENCES

1. S. Krishna, S. Raghavan, G. von Winckel, A. Stintz, G. Ariyawansa, S.G. Matski, A.G.U. Perera, Appl. Phys. Lett., 83, (2003), 2746.

2. V. Ryzhii, V. Pipa, I. Khmyrova, V. Mitin, M. Willander, Japan. J. Appl. Phys., 39, (2000), L1283.

3. V. Ryzhii, I. Khmyrova, V. Mitin, M. Stroscio, M. Willander, Appl. Phys. Lett., 78, (2001), 3523.

4. J. Phillips, J. Appl. Phys., 91, (2002), 4590.

5. M.A. Kinch, J. Electronic Materials, 29, (2000), 809.

6. J. Bloch, J. Shah, W.S. Hobson, J. Lopata, S.N.G. Chu, Appl. Phys. Lett., 75, (1999), 2199

7. E.C. Le Ru, P. Howe, T.S. Jones, R. Murray, Phys. Rev. B, 67, (2003), 165303.

8. A. Passaseo, et. al., Appl. Phys. Lett., 78, (2001), 1382.

9. Z. Yuan, et. al., Science, 295, (2002), 102

10. P. Bhattacharya, et. al., Appl. Phys. Lett., 86, (2005), 191106.

11. S. Raghavan, et. al., Appl. Phys. Lett., 81, (2002), 1369.

12. J. Johansson, W. Seifert, J. Crystal Growth, 234, (2002), 132.

13. J. Johansson, W. Seifert, J. Crystal Growth, 234, (2002), 139.

14. T.J. Kryzewski, P.B. Joyce, G.R. Bell, T.S. Jones, Phys. Rev. Lett., 66, (2002), 201302

15. W.B. Yu, A. Madhukar, Phys. Rev. Lett., 79, (1997), 905.

16. V.A. Shchukin, et. al., Phys. Rev. Lett., 75, (1995), 2968.

17. I. Daruka, A-L. Barabási, Phys. Rev. Lett., 79, (1997), 3708.

18. R.E. Rudd, et. al., Phys. Rev. Lett., 90, (2003), 146101.

19. J.G. Cederberg, F.H. Kaatz, R.M. Biefeld, J. Crystal Growth, 261, (2004), 197.

20. J. Drucker, Phys. Rev. B, 48, (1993), 18203.

APPENDIX A: METRICS

- **Publications**
  - – Self-assembled quantum dot formation during the growth of $In_{0.4}Ga_{0.6}As$ on GaAs(001) by metal-organic vapor phase epitaxy: The role of In segregation, Journal of Crystal Growth, **307**, (2007), 44.
  - – Thermodynamic modeling of island size distributions for InGaAs/GaAs self-assembled quantum dots: a quantitative effort to understand ensemble size nonuniformity, submitted to the Journal of Applied Physics
- **Active Collaborations:**
  - – Sanjay Krishna (University of New Mexico, CHTM)
  - – Alexana Roshko (NIST - Boulder)

DISTRIBUTION

1	MS1427	J.M. Phillips	1100
1	MS1086	D.L. Barton	1123
1	MS1415	E.A. Shaner	1123
1	MS1086	J.G. Cederberg	1126
1	MS1086	R.M. Biefeld	1126
1	MS1082	F.B. McCormick	1727
1	MS1082	A.R. Ellis	1727
1	MS0352	S.L. Shinde	1715
1	MS1153	J. Urayama	5444
1	MS0899	Technical Library (electronic copy)	9536
1	MS0123	D. Chavez, LDRD Office	1011